



Cite this: *Nanoscale*, 2024, **16**, 13551

## Surface chemistry altering electronic behaviour of liquid metal-derived tin oxide nanosheets†

Xiaotian Wei,<sup>a</sup> Chung Kim Nguyen,<sup>a</sup> Patrick D. Taylor,<sup>b</sup> Vaishnavi Krishnamurthi,<sup>a</sup> Nitu Syed,<sup>a,d</sup> Phuong Y. Le,<sup>b</sup> Michelle J. S. Spencer,<sup>c</sup> Torben Daeneke<sup>\*a</sup> and Lei Bao<sup>id</sup><sup>\*a</sup>

Possessing excellent electronic properties and high chemical stability, semiconducting n-type two-dimensional (2D) tin dioxide (SnO<sub>2</sub>) nanosheets have been featured in sensing and electrocatalysis applications recently. Derived from non-layered crystal structures, 2D SnO<sub>2</sub> has abundant unsaturated dangling bonds existing at the surface, providing interfacial activity. How the surface chemistry alters the electronic properties of 2D SnO<sub>2</sub> nanomaterials remains unexplored. In this study, we synthesised ultra-thin 2D SnO<sub>2</sub> nanosheets using a liquid metal (LM) touch printing technique and investigated experimentally and theoretically how the interactions of organic solvents composed of alkyl and hydroxyl groups with the surface of LM-derived 2D SnO<sub>2</sub> modulate the electronic properties. It was found that alkane solvents can physically absorb onto the SnO<sub>2</sub> surface with no impact on the material conductivity. Alcohol-based solvents on the other hand interact with the SnO<sub>2</sub> surface *via* chemical absorptions primarily, in which oxygen atoms of hydroxyl groups in the alcohols form bonds with the surface atoms of SnO<sub>2</sub>. The binding stability is determined by the length and configuration of the hydrocarbon chain in alcohols. As representative long-chain alcohols, 1-octanol and 1-pentanol attach onto the SnO<sub>2</sub> surface strongly, lowering the binding energy of Sn<sup>4+</sup> and reducing the electron transfer ability of SnO<sub>2</sub> nanosheets. Consequently, the electronic properties, *i.e.* conductivity and electronic mobility of SnO<sub>2</sub> nanosheet-based electronic devices are decreased significantly.

Received 29th April 2024,  
 Accepted 26th June 2024

DOI: 10.1039/d4nr01841a

rsc.li/nanoscale

### 1. Introduction

Two-dimensional (2D) metal oxides (MOXs) are emerging ultra-thin semiconducting materials, advancing technology in many areas including electronics,<sup>1–3</sup> sensing,<sup>4–6</sup> catalysis<sup>7</sup> and energy storage.<sup>8</sup> Among different synthesis approaches, the recently developed liquid metal (LM) technique harvests oxide skins from the surface of low-melting-point metals, signifying a versatile method for high-quality and large-scale 2D MOX production.<sup>9</sup> This straightforward and cost-effective method hinges on the self-limiting surface oxidation of post-transition metals and their alloys, following the Cabrera–Mott oxidation model.<sup>10–13</sup> Through this approach, both stratified and unstratified MOXs have been successfully fabricated, showcasing enhanced properties applicable to electronics, optics, sensing, and catalysis.<sup>9,14–18</sup>

As representative 2D unstratified semiconducting oxides, tin dioxide (SnO<sub>2</sub>) nanosheets are of technological interest due to their low cost, wide bandgap, excellent electronic properties, and high chemical stability. Utilising the LM method, ultra-thin 2D SnO<sub>2</sub> films with an area of several square millimetres have been exfoliated and deposited directly on solid and flexible substrates under atmospheric conditions.<sup>19</sup> The as-obtained SnO<sub>2</sub> nanosheets displayed parts-per-billion level sensitivity as well as excellent selectivity towards ammonia gas with and without UV-light stimulus. The underlying mechanism was attributed to the electron transfer as well as interfacial interactions between LM-derived n-type SnO<sub>2</sub> nanosheets and gas molecules. The LM method can also be modified to produce colloidal SnO<sub>x</sub> nanosheets suspended in solutions for electrocatalytic CO<sub>2</sub> conversion.<sup>20,21</sup> A gas-injection strategy was applied, in which oxygen or air was bubbled into liquid Sn to strip off amorphous 2D SnO<sub>x</sub> nanoflakes into selected solvents. It was found that the interactions between solvent molecules and surface oxides are key to the morphology of as-formed SnO<sub>x</sub>. Solvents rich in hydroxyl groups tended to

<sup>a</sup>School of Engineering, RMIT University, Australia.

E-mail: torben.daeneke@rmit.edu.au, lei.bao@rmit.edu.au

<sup>b</sup>School of Science, RMIT University, Australia

<sup>c</sup>ARC Centre of Excellence in Future Low-Energy Electronics Technologies, School of Science, RMIT University, Australia

<sup>d</sup>ARC Centre of Excellence for Transformative meta-Optical Systems, The University of Melbourne, Australia

† Electronic supplementary information (ESI) available. See DOI: <https://doi.org/10.1039/d4nr01841a>

absorb on the SnO<sub>2</sub> surface strongly, favouring SnO<sub>2</sub> nanoflake formation and stabilisation. It is notable that besides the intrinsic semiconducting nature, surface chemistry is also vital to the material physiochemical properties and applications of LM-derived 2D SnO<sub>2</sub>.

Distinguished from the wet-chemistry approach, where SnO<sub>2</sub> nanostructures are generated by bottom-up reactions from precursors,<sup>22</sup> the developed LM method is considered as a top-down strategy, where SnO<sub>2</sub> nanosheets can be simply exfoliated from the bulk material, *i.e.* oxidised liquid Sn.<sup>19</sup> The resulting 2D SnO<sub>2</sub> is composed of covalent bonds at all dimensions and abundant unstratified dangling bonds on the surface, offering active sites for interfacial interactions. Although the current LM processes have been proven effective in creating 2D SnO<sub>2</sub> with superior properties for gas sensing and electronics,<sup>19,23–25</sup> understanding the interfacial chemistry of as-produced SnO<sub>2</sub> is limited. In particular, the influence of intrinsic electronic properties of produced 2D SnO<sub>2</sub> by surface chemistry remains unexplored.

It is known that 2D layered van der Waals (vdW) materials' properties, such as electrochemical activities, friction and conductivity, can be tailored by attaching hydrocarbon molecules onto the surface.<sup>26</sup> Organic molecules have served as dopants to change charge carrier concentration in graphene and 2D transition-metal dichalcogenide (TMD) materials, endowing tunable electrical characteristics.<sup>27</sup> However, little has been done to understand and modulate the electrical properties of non-layered 2D metal oxides, SnO<sub>2</sub> in particular, by the surface decoration of organic molecules.

In this study, we deposit several organic solvents onto LM-printed ultra-thin SnO<sub>2</sub> nanosheets and investigate the effects of alkyl and hydroxyl groups on the electronic properties of the 2D SnO<sub>2</sub>. The conductivity and electron mobility of the SnO<sub>2</sub> nanosheets before and after solvent molecular absorption were evaluated based on corresponding two-terminal conductometric devices and field-effect transistors (FETs). The interfacial interactions between the solvent molecules and dangling bonds of the SnO<sub>2</sub> nanosheets were revealed by X-ray photoelectron spectroscopy (XPS) and Raman spectroscopy. Density functional theory (DFT) calculations were employed to provide an in-depth understanding of the binding orientation and strength. The presented study provides insights into the interfacial interactions between organic molecules and outermost atoms of LM-derived 2D SnO<sub>2</sub>, amplifying the crucial impact of surface chemistry on the electronic properties of semiconducting 2D MOXs. Moreover, this work implicates the importance of solvent selection in producing high quantity unstratified 2D MOXs as well as hinting at the potential for tuning electronic properties of 2D MOXs by surface doping of organic molecules.

## 2. Experimental section

### 2.1 Materials

Tin (Sn, 99.9% purity) was purchased from Roto Metals. All organic solvents including ethanol, acetone, 1-octanol, 1-penta-

anol, and dodecane in HPLC grade were purchased from Sigma-Aldrich and used as received. 300 nm SiO<sub>2</sub>/p<sup>+</sup> Si wafers were purchased from D&X Co., Ltd.

### 2.2 Synthesis of 2D SnO<sub>2</sub> nanosheets

300 nm thick SiO<sub>2</sub>/p<sup>+</sup> Si substrates were prepared by cleaning with acetone, isopropanol, and Milli-Q water, and dried using compressed air. Ultra-thin SnO<sub>2</sub> nanosheets were synthesised by the touch printing method as per previous reports.<sup>28</sup> Before synthesis, 300 nm SiO<sub>2</sub>/Si substrates were preheated on a hot plate at 300 °C to remove contamination residuals. Solid tin metal was placed on a glass slide and heated to a molten state. Preheated glass pieces of size 2 × 2 cm were prepared to squeeze the liquid Sn metal to remove the thick oxide layer. The preheated substrate was carefully picked up by a tweezer and touched the surface of molten liquid metal, which aided in exfoliating 2D tin oxide nanosheets from the liquid metal. To get 2D SnO<sub>2</sub> samples, all printed 2D SnO<sub>x</sub> samples were then annealed at 450 °C for 15 minutes. For TEM samples, 2D SnO<sub>2</sub> was directly produced onto silicon nitride TEM grids *via* the aforementioned procedure.

### 2.3 Solvent-treated SnO<sub>2</sub> nanosheets

50 μL of organic solvents were drop-casted onto SnO<sub>2</sub> nanosheets, which were then placed facing up and dried in a vacuum oven at 40 °C for 8 hours.

### 2.4 Characterisation

All optical images of vdW exfoliated 2D SnO<sub>2</sub> nanolayers were taken under a Leica DM2500 optical microscope. The surface morphology and thickness of 2D SnO<sub>2</sub> nanosheets were determined with a Bruker Dimension Icon atomic force microscope (AFM) operating under the ScanAsyst-Air mode. The collected data was then processed and analysed using the Gwyddion 2.55 software. TEM images were taken using a JEOL-2100F TEM operating at an acceleration voltage of 200 kV equipped with a Gatan Orius SC100 CCD camera. XPS was carried out with Thermo Scientific K-alpha XPS spectrometer features a monochromatic (Al Kα) X-ray source with an energy of 1486.7 eV and a concentric hemispherical electron analyser operated with a pass energy of 50 eV. The XPS data were calibrated with C 1s at 284.8 eV and processed with CasaXPS software. Raman spectroscopy was obtained from the Horiba Scientific LabRAM HR evolution Raman spectrometer using a 50× objective, 1800 mm<sup>-1</sup> grating, and 532 nm laser delivering 9 mW to the sample synthesised on a silicon wafer. The sample tested for Raman spectra was multi-touch printed to gain enough signals.

### 2.5 Electronic device fabrication

The FET and two-terminal devices were fabricated *via* a photolithography process. First, the AZ 5214E photoresist was spin-coated on ultra-thin SnO<sub>2</sub> nanosheets covered SiO<sub>2</sub>/p<sup>+</sup> Si substrates prior to the electrode patterning using a Maskless Aligner – Heidelberg MLA150. The channel areas of FETs are 40 × 20 μm<sup>2</sup>. An e-beam evaporator (PVD75 – Kurt J. Lesker)

was then employed to deposit Cr/Au (10/100 nm) electrodes, followed by a lift-off process utilising acetone to remove the photoresist residue. The exposed working areas of SnO<sub>2</sub> nanosheets on either FET or two-terminal devices were then modified by organic solvents following the protocols described in the previous section.

## 2.6 Device performance measurements

Device measurements were performed using a probe station equipped with a Keysight B2902A Precision Source/Measure Unit (SMU). The active channel of the formulated two-terminal devices was considered to be the length and width between the electrodes with some slight effects from fringing currents. The drain–source current ( $I_{DS}$ ) versus drain–source voltage ( $V_{DS}$ ) of the devices was measured when the gate–source voltage ( $V_{GS}$ ) varied from  $-40$  to  $40$  V in the FETs. FET mobility was subsequently calculated by using the following equation.

$$\mu_e = \frac{L}{W} \frac{dI_{DS}}{dV_{GS}} \frac{1}{V_{DS} C_{OX}} \quad (1)$$

where  $\mu_e$  is the electron mobility ( $\text{cm}^2 \text{V}^{-1} \text{s}^{-1}$ ),  $L$  refers to the active channel length ( $= 20 \mu\text{m}$ ) and  $W$  is the active channel width ( $= 40 \mu\text{m}$ ).  $I_{DS}$  and  $V_{DS}$  are the drain–source current and voltage, respectively.  $dI_{DS}/dV_{GS}$  is the slope of the high  $V_{GS}$  region of the transfer curve. To prevent devices from being burnt out under high voltages,  $V_{DS}$ , drain voltage in the test is set to be  $1$  V for stable measurements.<sup>29,30</sup>  $C_{OX}$ , the gate insulator capacitance per unit area is  $11.5 \times 10^{-9} \text{F cm}^{-2}$  for  $300 \text{nm SiO}_2$ .<sup>23,49</sup>

## 2.7 DFT calculations

The quantum mechanical calculations were performed using DFT as implemented in the Vienna *ab initio* Simulation Package (VASP).<sup>31,32</sup> The generalised-gradient approximation (GGA) was employed with the Perdew–Burke–Ernzerhof (PBE)<sup>33</sup> exchange–correlation functional and projector-augmented wave (PAW)<sup>34</sup> method to define the ion–electron interaction. An energy cut-off of  $400 \text{eV}$  was used, with a  $k$ -point mesh of  $5 \times 5 \times 1$  for the geometry optimizations and  $1 \times 1 \times 1$  for the *ab initio* molecular dynamic (AIMD) simulations to sample the Brillouin zone. vdW forces were accounted for by the Grimme DFT-D3 approach.<sup>35</sup> The AIMD simulations were performed at  $298 \text{K}$  with a time step of  $0.5 \text{fs}$  for up to  $3.8 \text{ps}$ .

The SnO<sub>2</sub>(110) surface was cleaved from bulk SnO<sub>2</sub> with cell dimensions of  $4.83 \times 4.83 \times 3.24 \text{Å}$ , which agrees with a previous DFT study.<sup>36</sup> The (110) facet was selected as it is the most thermodynamically stable surface.<sup>37,38</sup> A  $[4 \times 2]$  model was used, having lattice parameters of  $a = 12.97 \text{Å}$  and  $b = 13.67 \text{Å}$ . A vacuum spacer of  $20 \text{Å}$  was added in the  $z$ -direction to minimize interactions between adjacent cells after applying periodic boundary conditions. To represent the defect surface, one of the topmost surface O atoms was removed from the stoichiometric surface, creating the SnO<sub>2</sub>(110)–V<sub>O</sub> surface. To model the adsorption of octanol on the surface, the adsorbate was initially placed  $\sim 3 \text{Å}$  above each surface in different locations above the surface and in different orientations. The atoms in the bottom surface layer were fixed while all other atoms were allowed to

relax until the total energy of the system was converged to  $1 \times 10^{-6} \text{eV}$  and the Hellman–Feynman force on each relaxed atom was less than  $0.01 \text{eV Å}^{-1}$ . The binding energies were calculated as  $\text{BE} = (E_{\text{octanol+surface}} - E_{\text{surface}} - E_{\text{octanol}})$ , where  $E_{\text{octanol+surface}}$ ,  $E_{\text{surface}}$ , and  $E_{\text{octanol}}$  are the total energies of the adsorbed system, the isolated surface and the isolated octanol, respectively. The octanol molecule was optimised in a  $30 \times 30 \times 30 \text{Å}^3$  sized cell using a  $k$ -point mesh of  $1 \times 1 \times 1$ .

# 3. Results and discussion

## 3.1. Formation of SnO<sub>2</sub> nanosheets by LM method

Ultra-thin tin oxide nanosheets were synthesised by the LM process as illustrated in Fig. 1(a). Briefly, the initial step involves heating the tin metal to its liquid phase, followed by contacting with a flat preheated SiO<sub>2</sub> substrate. Since the heating process took place under atmospheric conditions, it resulted in the formation of interfacial tin oxide layers over the tin metal. The attachment between the tin metal and the interfacially formed tin oxides is relatively weak. In comparison, vdW interactions between the solid substrate and the interfacial oxide layer are stronger, enabling the tin oxide nanosheets to be detached from the tin metal surface and subsequently forming ultra-thin layers on a solid substrate.<sup>20</sup>

The obtained pristine SnO<sub>x</sub> nanosheets were examined under an optical microscope shown in Fig. S1(a).† The different reflection colour displayed under the optical microscopy depicts the successful delamination of tin oxide nanosheets (blue colour), which have been transferred onto SiO<sub>2</sub> substrates (purple colour). This finding, in conjunction with previous reports in the literature,<sup>21,28,39–41</sup> suggests the feasibility of exfoliating ultra-thin tin oxide nanosheets by LM. Large-scale fabrication with lateral dimensions reaching millimetre scales is also achievable (Fig. S1(b)†), demonstrating the potential for integrating 2D materials into semiconductor manufacturing.<sup>24,42–46</sup> Further characterisation by XPS reveals that the as-synthesised SnO<sub>x</sub> nanosheets contain a mixture of Sn<sup>2+</sup> and Sn<sup>4+</sup> oxidation states, indicating a degree of chemical inhomogeneity in the structure (Fig. S2†).

Thermal annealing was then applied to treat the as-synthesised SnO<sub>x</sub> nanosheets. After being heated at  $450 \text{°C}$  for  $15 \text{minutes}$  in the air, the sample was re-examined under the optical microscope. Its colour became lighter as depicted in Fig. 1(b). The high-resolution morphology of the annealed samples is visualised through AFM in Fig. 1(c) and Fig. S3,† showing a smooth and flat nanosheet with a thickness of  $2.68 \pm 0.34 \text{nm}$ . The XPS spectra of Sn 3d in Fig. 1d show Sn 3d<sub>3/2</sub> peaking at the binding energies of  $494.9 \text{eV}$  and Sn 3d<sub>5/2</sub> at  $486.9 \text{eV}$ . The deconvolution of these two peaks reveals dominating Sn<sup>4+</sup> chemical characteristics in the annealed samples. Raman spectroscopy was also employed to characterise the annealed SnO<sub>x</sub> nanosheets (Fig. 1(e)). The peak at  $618 \text{cm}^{-1}$  presents the A<sub>1g</sub> mode of the tetragonal rutile structure of SnO<sub>2</sub> crystals with the existence of bridging oxygen vacancies.<sup>47</sup> TEM images of annealed SnO<sub>x</sub> in Fig. 1(f) reveal a

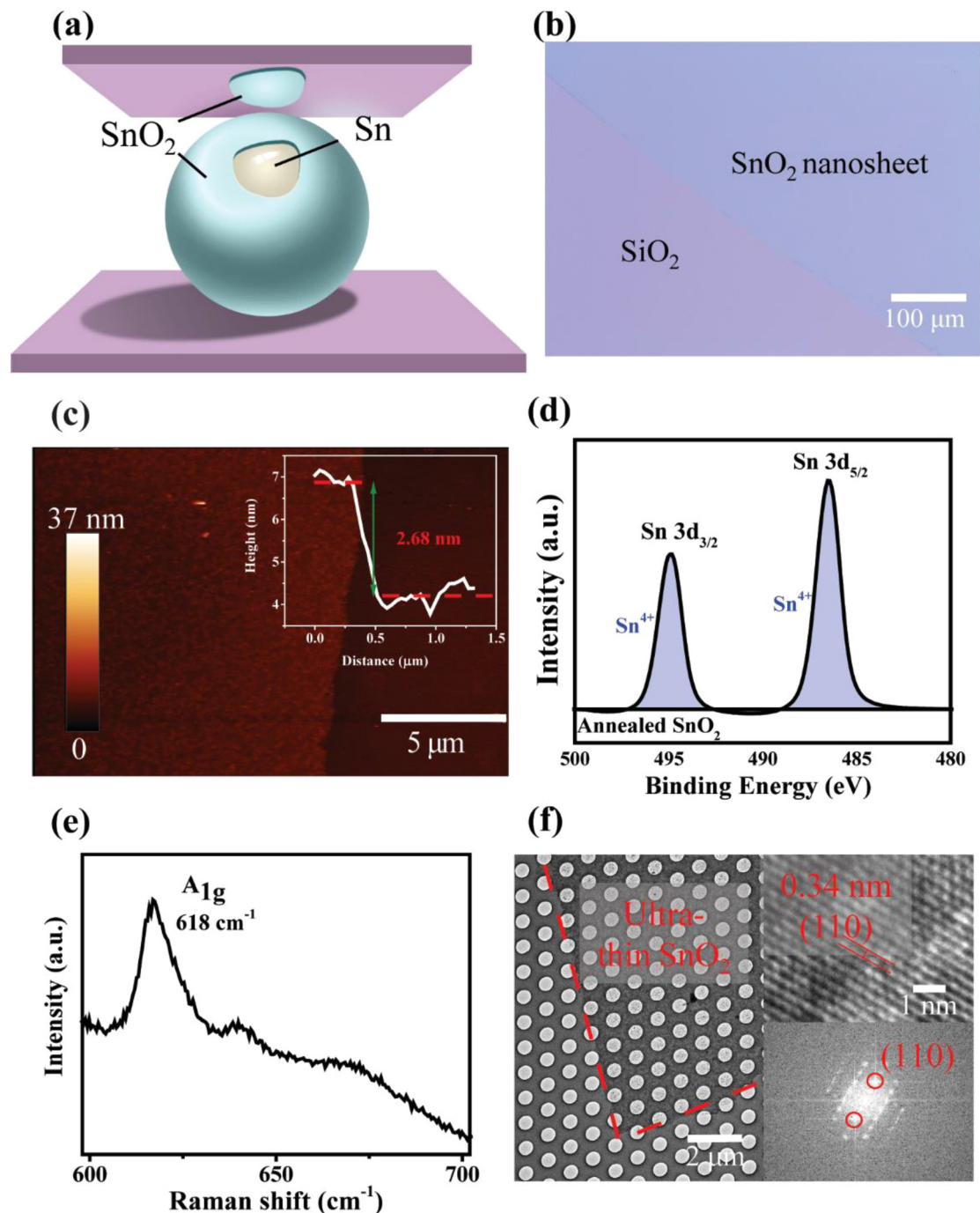


**Fig. 1** High-quality SnO<sub>2</sub> nanosheets by the LM touch printing method. (a) Schematic illustration of ultrathin SnO<sub>2</sub> nanosheets forming on the SiO<sub>2</sub> substrate. (b) Optical image of obtained SnO<sub>2</sub> nanosheet on SiO<sub>2</sub> (300 nm)/Si substrate. (c) AFM image of a SnO<sub>2</sub> nanosheet with the corresponding step height profile (top right inset). (d) XPS spectrum in the Sn 3d region of the SnO<sub>2</sub> nanosheet. (e) Raman spectrum of a SnO<sub>2</sub> nanosheet. (f) TEM (left), HRTEM (top right), and the corresponding FFT (bottom right) images of the SnO<sub>2</sub> nanosheet.

homogeneous appearance with a *d*-spacing of 0.34 nm, corresponding to the (110) index of SnO<sub>2</sub> crystals, as corroborated by the fast Fourier transforms (FFT) analysis. It was confirmed that after the annealing process, SnO<sub>x</sub> has been transitioned into SnO<sub>2</sub>. Therefore, the obtained annealed SnO<sub>x</sub> nanosheets are noted as SnO<sub>2</sub> in the following studies.

### 3.2. Electronic performance of solvent-treated SnO<sub>2</sub> nanosheets

The high-quality and large-scale SnO<sub>2</sub> nanosheets generated on silica substrates allow to fabricate electronic devices conveniently. As illustrated in Fig. 2(a), SnO<sub>2</sub>-based two terminal

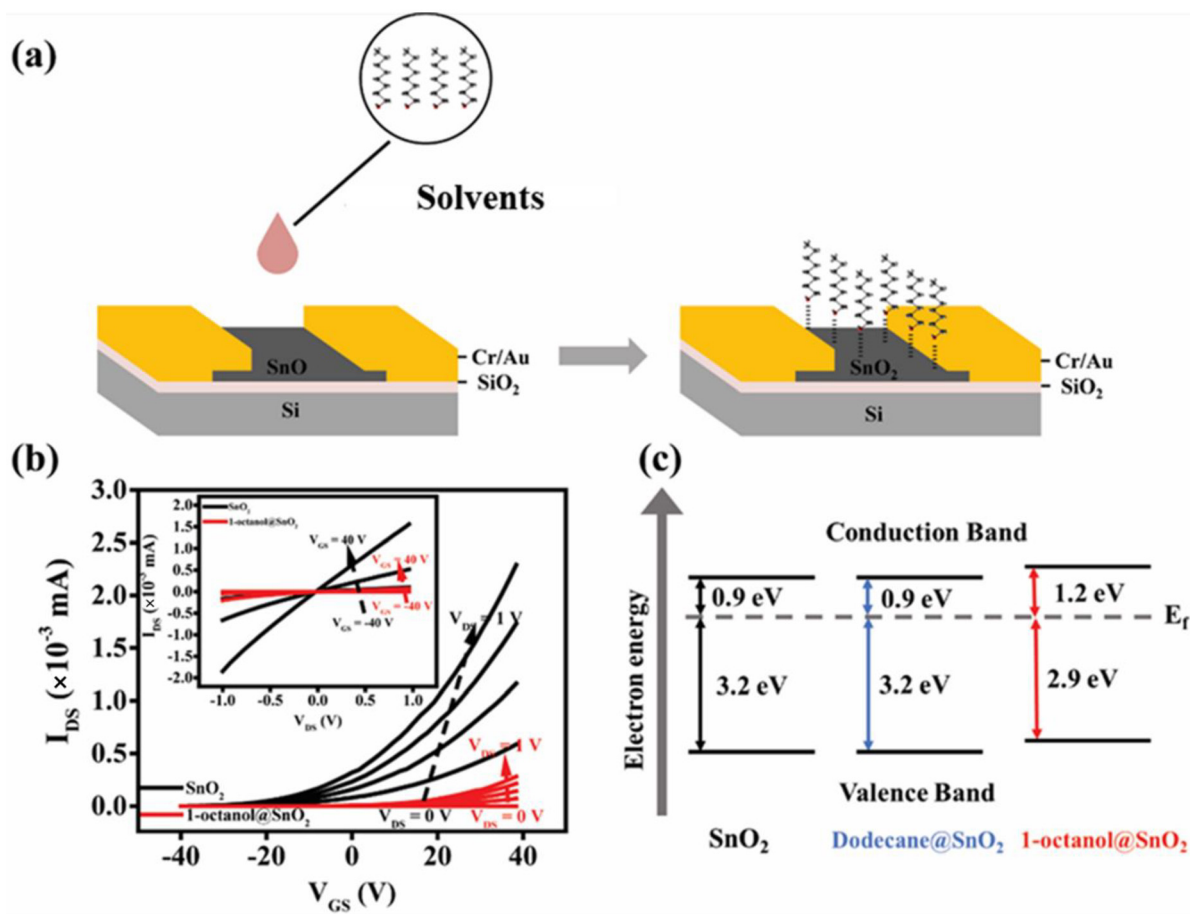


**Fig. 2** Electronic performance of solvent-treated SnO<sub>2</sub> surface. (a) A schematic illustration of coating solvents onto SnO<sub>2</sub>-based FET electronic devices device. (b) Transfer curves of FET devices based on annealed SnO<sub>2</sub> nanosheets before (black) and after (red) applying 1-octanol with  $V_{DS}$  ranging from 0 to 1 V. The inset in (b) shows the output curves of the FET device based on annealed SnO<sub>2</sub> nanosheets before (black) and after (red) applying 1-octanol with varying  $V_{GS}$  from  $-40$  to  $40$  V. (c) Simplified band diagrams of SnO<sub>2</sub>, 1-octanol@SnO<sub>2</sub>, and dodecane@SnO<sub>2</sub>, respectively.

devices/FETs were constructed. The solvent molecules were then deposited onto the surface of SnO<sub>2</sub> afterwards. The electronic behaviours of the SnO<sub>2</sub> before and after the solvent coating were assessed and compared.

The current–voltage ( $I$ – $V$ ) curves of SnO<sub>2</sub>-based devices were tested initially. When applying dodecane onto SnO<sub>2</sub>, there was a negligible change in  $I$ – $V$  behaviour (Fig. S4†). However, when the surface of SnO<sub>2</sub> was exposed to 1-octanol, unexpectedly higher electric resistance was displayed on 1-octanol@SnO<sub>2</sub> devices compared to SnO<sub>2</sub> devices (Fig. S5†). To investigate this further, back-gated FET devices were constructed. The SnO<sub>2</sub> nanosheet-based transistor exhibited exceptional electronic performance, attributed to fast electron mobility and high conductivity of LM-derived 2D SnO<sub>2</sub>.<sup>23</sup> The output curves ( $I_{DS}$  vs.  $V_{DS}$ ) and transfer curves ( $I_{DS}$  vs.  $V_{GS}$ ) plotted in Fig. 2(b), respectively, confirmed the n-type semiconducting behaviour of SnO<sub>2</sub> nanosheets<sup>48</sup> with electron mobility  $\mu_e$  of  $2.2 \text{ cm}^2 \text{ V}^{-1} \text{ s}^{-1}$ . Upon applying 1-octanol onto SnO<sub>2</sub>, it is pronounced to see the significant alterations in the FET device performance. Both  $I_{DS}$ – $V_{DS}$  and  $I_{DS}$ – $V_{GS}$  profiles of the devices exhibited a significant reduction in the drain current. At  $V_{GS} = 40$  V and

$V_{DS} = 1$  V,  $I_{DS}$  decreased from  $1.56 \mu\text{A}$  to  $0.08 \mu\text{A}$  as shown in Fig. 2(b) insert, indicating a huge drop in  $\mu_e$ . Although it retained n-type semiconducting behaviour after 1-octanol coated on the SnO<sub>2</sub> surface,  $\mu_e$  of 1-octanol@SnO<sub>2</sub> FET was calculated to be  $0.3 \text{ cm}^2 \text{ V}^{-1} \text{ s}^{-1}$ . An 86% reduction in electron mobility suggests a compromised performance when the SnO<sub>2</sub> surface is covered by 1-octanol molecules. The on/off ratio of the device was also decreased from  $2.45 \times 10^3$  to  $8.93 \times 10^2$ , which is consistent with observation on the  $I$ – $V$  characteristics.

It is known that the electron mobility of the n-type semiconductor is influenced by the position of the Fermi level ( $E_f$ ) to the conductive band.<sup>46</sup> To construct the band diagram, Tauc plots of these samples were extracted from UV-vis absorption spectra first. By extrapolating the linear part, the optical bandgaps for all the samples are found to remain at  $\sim 4.1$  eV (Fig. S6(a)†). XPS valence band analysis (VB-XPS) was performed as well. The Fermi level positions relative to their valence band edge were determined by extrapolating the onset of the leading edge of the VB-XPS (Fig. S6(b)†). They are observed to be 3.2 eV for both SnO<sub>2</sub> nanosheets and the dodecane-treated ones, while 2.9 eV for

the 1-octanol-treated SnO<sub>2</sub> nanosheets. Accordingly, the simplified electronic band structures of these three samples are provided in Fig. 2(c). Notably, the Fermi level of SnO<sub>2</sub> shifts away from its conduction band when 1-octanol was capped onto the surface, enlarging the barrier for electrons in the valence band to transition into the conduction band.<sup>49</sup> On the other hand, it is possible that the interaction between 1-octanol and the SnO<sub>2</sub> surface results in distortion of the SnO<sub>2</sub> crystal lattice and reduction of overall electron concentrations.<sup>19</sup> As a result, the electronic performance of SnO<sub>2</sub>-based devices is suppressed.

### 3.3 Surface states of solvent-treated SnO<sub>2</sub> nanosheets

It is evident that the electronic properties of SnO<sub>2</sub> were sensitive to surface. To probe the surface chemistry of the aforementioned organic molecule treated SnO<sub>2</sub>, XPS as a surface-sensitive technique, was deployed.<sup>50</sup> The high-resolution survey of the Sn 3d in Fig. 3(a) showed that the Sn 3d<sub>5/2</sub> peak of the SnO<sub>2</sub> was at 486.9 eV initially. After the deposition of dodecane onto SnO<sub>2</sub> nanosheets, a subtle shift of 0.1 eV in the Sn 3d<sub>5/2</sub> peak occurred. As for 1-octanol-treated SnO<sub>2</sub>, a more pro-

nounced shift toward a low binding energy in the Sn 3d<sub>5/2</sub> peak, to 486.6 eV, was observed. Such a shift suggests an increase in the electron density around Sn atoms, resulting from the change in Sn atom binding states.<sup>51</sup> The normalised carbon-to-tin (C:Sn) ratios are 0.24 and 0.26 for dodecane@SnO<sub>2</sub> and 1-octanol@SnO<sub>2</sub> (Fig. 3(b)), respectively, suggesting ~0.02 dodecane molecule per Sn atom and ~0.031-octanol molecules per Sn atom on the SnO<sub>2</sub> surface. Notably, with similar coverage on SnO<sub>2</sub>, 1-octanol, containing the OH group, displayed much stronger interactions with Sn atoms than dodecane, consequently altering the electronic properties of SnO<sub>2</sub>.<sup>52</sup> We also conducted tests with other alkane solvents including decane and hexadecane, which showed no impact on the Sn 3d<sub>5/2</sub> peak energy (Fig. 3(b)). As for other primary alcohols including ethanol and 1-pentanol, interestingly, ethanol has little impact on *I-V* characteristics (see Fig. S7†) and the Sn 3d<sub>5/2</sub> peak energy of SnO<sub>2</sub>. While similar to 1-octanol, 1-pentanol made the electric resistance of SnO<sub>2</sub> increase (see Fig. S8†), and the Sn 3d<sub>5/2</sub> peak shifted 0.3 eV to a low energy side. The results herein signify the roles of both the alkyl chain and the OH group in interacting with the SnO<sub>2</sub>

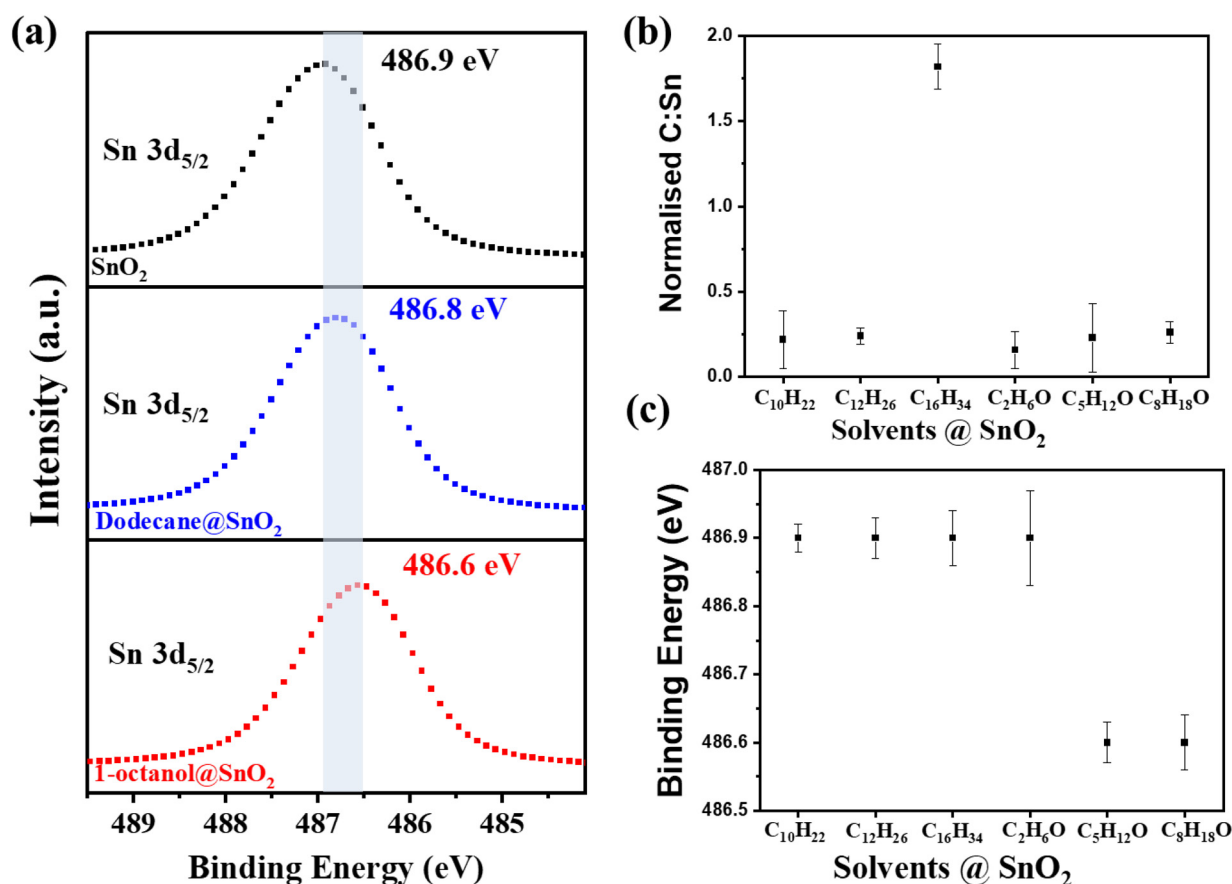


**Fig. 3** Surface characterisation of solvent-treated SnO<sub>2</sub>. (a) XPS spectra in the Sn 3d<sub>5/2</sub> region of the SnO<sub>2</sub> nanosheet, where the black represents pristine SnO<sub>2</sub>, the blue represents dodecane@SnO<sub>2</sub>, and the red represents 1-octanol@SnO<sub>2</sub>. (b) Normalised C:Sn ratios from SnO<sub>2</sub> treated by alkanes including decane (C<sub>10</sub>H<sub>22</sub>), dodecane (C<sub>12</sub>H<sub>26</sub>), and hexadecane (C<sub>16</sub>H<sub>34</sub>) as well as alcohols including ethanol (C<sub>2</sub>H<sub>6</sub>O), 1-pentanol (C<sub>5</sub>H<sub>12</sub>O) and 1-octanol (C<sub>8</sub>H<sub>18</sub>O). Note that the carbon-to-tin ratio of solvents@SnO<sub>2</sub> is normalised by the carbon-to-tin ratio obtained on the SnO<sub>2</sub> surface to provide a semi-quantitative estimation. (c) The binding energy of Sn 3d<sub>5/2</sub> in indicated solvent-treated SnO<sub>2</sub>.

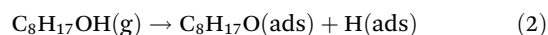
surface. It is considered that the OH group with unpaired electrons on its oxygen atom is capable of binding with Sn atoms and the alkyl chain can facilitate such interactions *via* physical absorption,<sup>19</sup> collectively suppressing the electronic mobility and conductivity of SnO<sub>2</sub>. The observed synergy impact of alcohol molecules on SnO<sub>2</sub> is regarded as the doping effect. Positive dipoles of the OH group are likely to induce the depletion of charge carriers in the SnO<sub>2</sub> conduction band, lowering charge mobilities and densities.<sup>53</sup> Meanwhile, the physisorbed long alkyl chain with a wide bandgap hinders efficient charge transfer.<sup>54</sup> Therefore, SnO<sub>2</sub> treated by 1-octanol and 1-pentanol exhibited pronounced Sn 3d<sub>5/2</sub> peak energy shift as well as a significant decrease in the electronic mobility and conductivity.

As for alkane molecules, unlike previously reported work on layered 2D materials, our results indicated that the physical absorption of these hydrocarbons has little impact on the Sn binding energy and SnO<sub>2</sub> electronic behaviours. Also, the influence of solvent volatility, which is reduced along with

increased hydrocarbon chains, cannot be excluded. Compared to 1-octanol and 1-pentanol, ethanol is more volatile and readily evaporates thus its contact with SnO<sub>2</sub> is relatively insufficient under the incubation condition with negligible influence.

### 3.4. Mechanism of 1-octanol interacting with SnO<sub>2</sub> surface

Elucidation of the binding mechanism between 1-octanol and SnO<sub>2</sub> nanosheets is expanded upon through the utilisation of DFT calculations and AIMD simulations, as presented in Fig. 4 and Fig. S9.† Both the pristine Sn surface (SnO<sub>2</sub>) and the surface with oxygen vacancies (SnO<sub>2</sub>-V<sub>O</sub>) were examined. Interestingly, 1-octanol was observed to preferentially adsorb dissociatively on both surfaces as follows:



The specific orientations of the 1-octanol molecule on each surface are illustrated in Fig. 4 and Table S1† summarises the binding energy (BE, eV), along with crucial bond distances

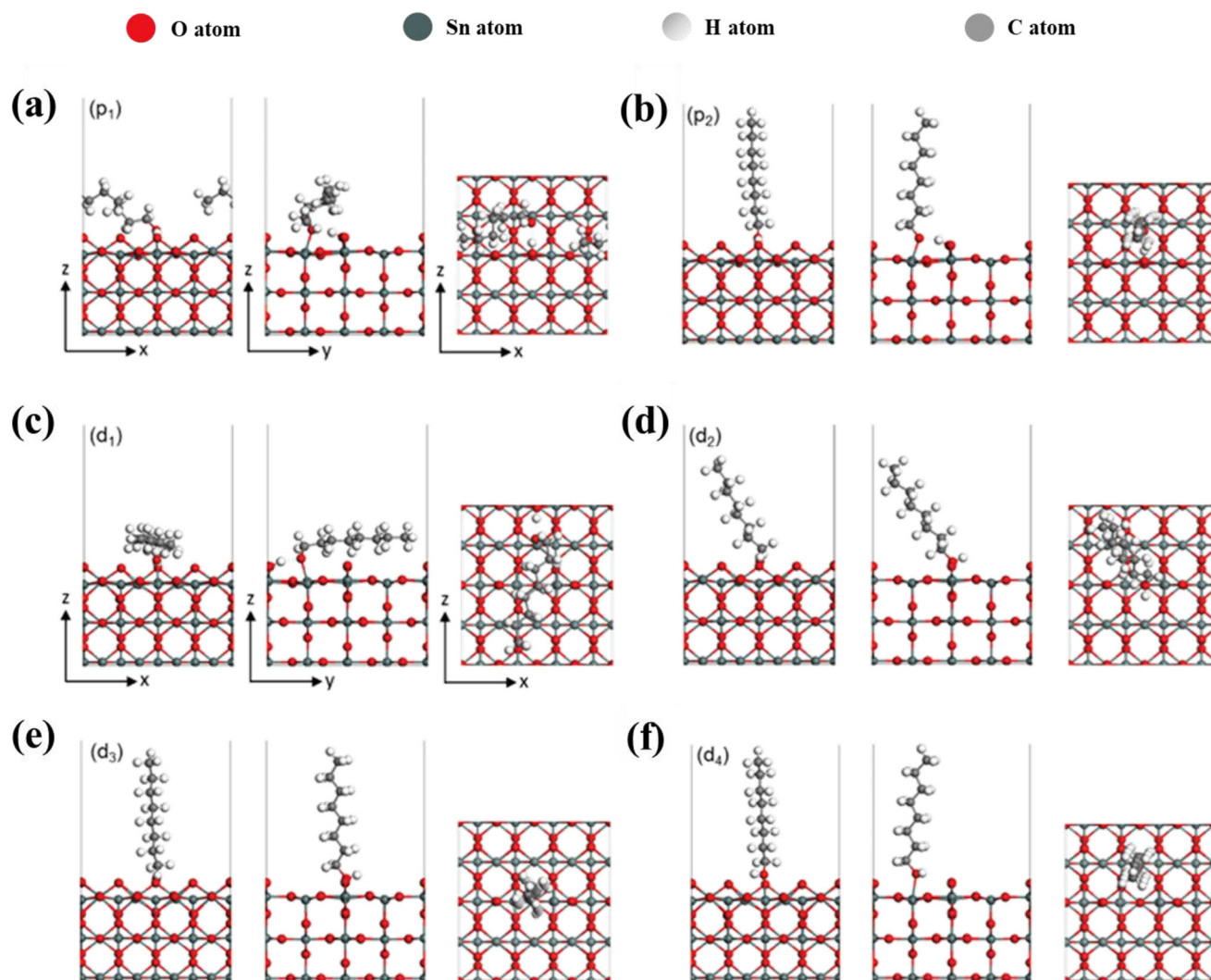


Fig. 4 Top and side views of stable configurations of 1-octanol interacting with SnO<sub>2</sub> surface *via* DFT modelling. (a and b) 1-octanol adsorbed on the stoichiometric SnO<sub>2</sub>(110) surface. (c–f) 1-octanol adsorbed on the SnO<sub>2</sub>(110)-V<sub>O</sub> surface.

( $d$ , Å), pertaining to the stable configurations of 1-octanol adsorbed onto the SnO<sub>2</sub> and SnO<sub>2</sub>-V<sub>O</sub> surfaces. In the case of the SnO<sub>2</sub> surface (Fig. 4(a and b)), there are two stable orientations with BE of  $-1.62$  eV for  $p_1$  and  $-1.54$  eV for  $p_2$ . For both structures, 1-octanol chemisorbs on the surface by its O atom binding to a surface Sn atom. This process causes the O–H bond to break, resulting H atom bonding to a neighbouring surface O atom on SnO<sub>2</sub>. The binding is also stabilised *via* formation of a hydrogen bond between the H and O atoms of the octanol. With a lower BE, structure  $p_1$  is regarded as more stable than structure  $p_2$  as the enhanced binding is achieved due to the alkyl chain being flat across the surface. For the SnO<sub>2</sub>-V<sub>O</sub> surface, four stable orientations were found with all structures chemisorbed having BE values of  $-2.24$ ,  $-1.21$ ,  $-1.19$ , and  $-1.07$  eV, respectively. Similar to the  $p_1$  structure on the SnO<sub>2</sub>, the most stable structure,  $d_1$ , binds to the SnO<sub>2</sub>-V<sub>O</sub> surface by breaking the O–H bond in the hydroxyl group and forming the O–Sn bond. The alkyl chain is also found to be flat along the surface. The binding is stronger than that in  $p_1$ . This is likely due to the different conformation of the hydrocarbon chain, which sits closer to the surface in  $d_2$ , enhancing its interaction with the surface. For  $d_2$ ,  $d_3$  and  $d_4$ , the OH bond remains intact, with 1-octanol adsorbing associatively. In  $d_2$  and  $d_3$ , the O atom of 1-octanol bonds to a Sn atom at the defect site while in  $d_4$ , it bonds to a surface Sn atom. Clearly, the orientation of the alkyl chain is vital to the binding strength. In comparison with  $d_1$ ,  $d_4$ , with a much lower BE, is less stable as its alkyl chain is oriented almost perpendicular to the surface.

Overall, the DFT findings are consistent with our experimental results, substantiating that the stable chemisorption between 1-octanol and the SnO<sub>2</sub> surface causes the distribution change of electron density on SnO<sub>2</sub>. While it is considered that the formation of a bond between octanol and the SnO<sub>2</sub> is essential for such a change, the conformation of the alkyl chain also matters to the binding stability. A horizontal alignment of the alkyl chain is much more favourable than a vertical alignment for enhancing the binding. Therefore, it is reasonable to see a subtle impact of ethanol onto the SnO<sub>2</sub> surface. Without stabilising from a long alkyl chain, the chemisorption of ethanol onto the SnO<sub>2</sub> is much weaker. Ethanol can easily dissociate from the surface binding, displaying negligible influence on the electronic properties of SnO<sub>2</sub>. While, the adsorption of 1-octanol onto SnO<sub>2</sub> is considerably stable and strong. Both  $I$ - $V$  characterisation and XPS measurements indicated partial restoration of the electronic performance of SnO<sub>2</sub> after 1-octanol@SnO<sub>2</sub> was treated by ethanol–acetone wash or thermal annealing (Fig. S10<sup>†</sup>).

## 4. Conclusion

In summary, we have investigated the impact of alkane solvents and primary alcohols on the electronic performance of LM technique-produced 2D SnO<sub>2</sub> nanosheets. Measurements of SnO<sub>2</sub>-based electronic devices confirmed that the electronic

performance of SnO<sub>2</sub> remained unchanged when exposed to alkane solvents but dropped significantly when in contact with non-volatile primary alcohols, such as 1-pentanol and 1-octanol. The electron mobility of FET devices fabricated using 1-octanol-modified SnO<sub>2</sub> only reached  $0.3 \text{ cm}^2 \text{ V}^{-1} \text{ s}^{-1}$ , far slower than that of SnO<sub>2</sub>-based FET devices. Combining XPS analysis with DFT modelling, it was ascertained that the adverse effect of non-volatile alcohol-based solvents on SnO<sub>2</sub> electronic properties was attributed to the formation of O–Sn bond between the OH group of the solvents and the surface Sn of SnO<sub>2</sub>, consequently changing the electronic band structure of SnO<sub>2</sub> and decreasing its electron mobility and density. Also, the binding stability and strength of alcohol solvents onto the SnO<sub>2</sub> surface are associated with the lengths and configuration of hydrocarbon chains in the alcohol molecules, which can potentially interfere with the charge transfer of SnO<sub>2</sub>. In contrast to ethanol, 1-octanol and 1-pentanol with long alkyl groups tended to strongly absorb on the SnO<sub>2</sub> surface with a preferred horizontal configuration of hydrocarbon chains. The experimental and theoretical results were consistent and provided an in-depth understanding of the interactions between organic molecules and unstratified 2D SnO<sub>2</sub>. The results imply that caution is necessary when using alcohol-based solvents to treat low-dimensional semiconductors, facilitating high-quality 2D MOX fabrication. More importantly, the work provided a strategy to switch the electronic characteristics of SnO<sub>2</sub> by doping alcohol molecules having different chain lengths, prompting the novel architecture design of responsive 2D MOX-based optoelectronic devices for sensing and detection applications.

## Data availability

The data supporting this article have been included as part of the ESI.<sup>†</sup>

## Author contributions

X.T.W.: methodology, investigation, writing – original draft, writing – review & editing, C.K.N.: methodology, analysis, investigation, writing – review & editing, P.D.T.: simulation, software, writing – original draft, writing – review & editing, V. K.: writing – original draft, writing – review & editing, N.S.: methodology, writing – review & editing, P.Y.L.: methodology, writing – review & editing, M.J.S.S.: supervision, simulation, writing – review & editing, T.D.: supervision, analysis, writing – review & editing, project administration, L.B.: conceptualisation, investigation, writing – original draft, writing – review & editing, supervision, project administration, funding acquisition.

## Conflicts of interest

The authors declare no conflict of interest.



## Acknowledgements

This work was performed in part at the RMIT Micro NanoResearch Facility (MNRF) in the Victorian Node of the Australian National Fabrication Facility (ANFF). The authors would also like to thank the RMIT Microscopy and Microanalysis Facility (RMMF). L. B. and X. W. acknowledge funding support from the Australian Research Council (ARC) DECRA program (DE190101514). T. D. and V. K., acknowledge funding from the ARC DP program (DP220101923). P. L. acknowledges financial support from the ARC DP program (DP200101905). N. S. recognises the support of a McKenzie Postdoctoral Fellowship from the University of Melbourne. P. T. acknowledges RMIT University for their RMIT Research Stipend Scholarship. This research was supported by the Australian Government's National Collaborative Research Infrastructure Strategy (NCRIS), with access to computational resources provided by the National Computational Infrastructure (NCI) Facility and the Pawsey Supercomputing Centre, through the National Computational Merit Allocation Scheme.

## References

- 1 Y. Gong, *et al.*, Two-Dimensional Hexagonal Boron Nitride for Building Next-Generation Energy-Efficient Devices, *ACS Energy Lett.*, 2021, **6**(3), 985–996.
- 2 F. H. Alshammari, M. K. Hota, Z. Wang, H. Al-jawhari and H. N. Alshareef, Atomic-Layer-Deposited SnO<sub>2</sub> as Gate Electrode for Indium-Free Transparent Electronics, *Adv. Electron. Mater.*, 2017, **3**(9), 1700155.
- 3 K. Mahmood, A. Khalid, F. Nawaz and M. T. Mehran, Low-temperature electrospray-processed SnO<sub>2</sub> nanosheets as an electron transporting layer for stable and high-efficiency perovskite solar cells, *J. Colloid Interface Sci.*, 2018, **532**, 387–394.
- 4 R. Zhuang, *et al.*, Solution-grown BiI/BiI(3) van der Waals heterostructures for sensitive X-ray detection, *Nat. Commun.*, 2023, **14**(1), 1621.
- 5 H. Mu, *et al.*, Interface and surface engineering of black phosphorus: a review for optoelectronic and photonic applications, *Mater. Futures*, 2022, **1**(1), 012301.
- 6 W. Wan, Y. Li, X. Ren, Y. Zhao, F. Gao and H. Zhao, 2D SnO<sub>2</sub> Nanosheets: Synthesis, Characterisation, Structures, and Excellent Sensing Performance to Ethylene Glycol, *Nanomaterials*, 2018, **8**(2), 112.
- 7 A. Bhattacharjee, S. Begum, K. Neog and M. Ahmaruzzaman, Facile synthesis of 2D CuO nanoleaves for the catalytic elimination of hazardous and toxic dyes from aqueous phase: a sustainable approach, *Environ. Sci. Pollut. Res.*, 2016, **23**(12), 11668–11676.
- 8 B. Saravanakumar and S.-J. Kim, Growth of 2D ZnO Nanowall for Energy Harvesting Application, *J. Phys. Chem. C*, 2014, **118**(17), 8831–8836.
- 9 P. Aukarasereenont, A. Goff, C. K. Nguyen, C. F. McConville, A. Elbourne, A. Zavabeti and T. Daeneke, Liquid metals: an ideal platform for the synthesis of two-dimensional materials, *Chem. Soc. Rev.*, 2022, **51**(4), 1253–1276.
- 10 X. Hu, K. Liu, Y. Cai, S.-Q. Zang and T. Zhai, 2D Oxides for Electronics and Optoelectronics, *Small Sci.*, 2022, **2**(8), 2200008.
- 11 K. Liu, H. Jin, L. Huang, Y. Luo, Z. Zhu, S. Dai, X. Zhuang, Z. Wang, L. Huang and J. Zhou, Puffing ultrathin oxides with nonlayered structures, *Sci. Adv.*, 2022, **8**(20), eabn2030.
- 12 T. Yang, T. T. Song, M. Callsen, J. Zhou, J. W. Chai, Y. P. Feng, S. J. Wang and M. Yang, Atomically Thin 2D Transition Metal Oxides: Structural Reconstruction, Interaction with Substrates, and Potential Applications, *Adv. Mater. Interfaces*, 2019, **6**(1), 1801160.
- 13 L. Yang-Yao, Novel Two-Dimensional Nanomaterial: High Aspect Ratio Titania Nanoflakes, in *Titanium Dioxide*, ed. Y. Dongfang, IntechOpen, 2018, ch. 2.
- 14 K. Zuraiqi, C. J. Parker, A. Zavabeti, A. J. Christofferson, S. Maniam, C. F. McConville, K. Chiang and T. Daeneke, Field's Metal Nanodroplets for Creating Phase-Change Materials, *ACS Appl. Nano Mater.*, 2022, **5**(5), 5952–5958.
- 15 C. K. Nguyen, A. Mazumder, E. L. H. Mayes, V. Krishnamurthi, A. Zavabeti, B. J. Murdoch, X. Guo, P. Aukarasereenont, A. Dubey, A. Jannat, *et al.*, 2 nm-Thick Indium Oxide Featuring High Mobility, *Adv. Mater. Interfaces*, 2023, **10**(9), 2202036.
- 16 V. Krishnamurthi, T. Ahmed, M. Mohiuddin, A. Zavabeti, N. Pillai, C. F. McConville, N. Mahmood and S. Walia, A Visible-Blind Photodetector and Artificial Optoelectronic Synapse Using Liquid-Metal Exfoliated ZnO Nanosheets, *Adv. Opt. Mater.*, 2021, **9**(16), 2100449.
- 17 X. Guo, C. K. Nguyen, A. Mazumder, Y. Wang, N. Syed, E. D. Gaspera, T. Daeneke, S. Walia, S. J. Ippolito, Y. Sabri, *et al.*, Gas sensors based on the oxide skin of liquid indium, *Nanoscale*, 2023, **15**(10), 4972–4981.
- 18 Y. Xia, L. Xu, S. He, L. Zhou, M. Wang, J. Wang and S. Komarneni, UV-activated WS<sub>2</sub>/SnO<sub>2</sub> 2D/0D heterostructures for fast and reversible NO<sub>2</sub> gas sensing at room temperature, *Sens. Actuators, B*, 2022, **364**, 131903.
- 19 C. K. Nguyen, P. D. Taylor, A. Zavabeti, H. Alluhaybi, S. Almalki, X. Guo, M. Irfan, M. A. Kobaisi, S. J. Ippolito, M. J. S. Spencer, *et al.*, Instant-in-Air Liquid Metal Printed Ultrathin Tin Oxide for High-Performance Ammonia Sensors, *Adv. Funct. Mater.*, 2023, 2309342.
- 20 A. Zavabeti, J. Z. Ou, B. J. Carey, N. Syed, R. Orrell-Trigg, E. L. H. Mayes, C. Xu, O. Kavehei, A. P. O'Mullane, R. B. Kaner, *et al.*, A liquid metal reaction environment for the room-temperature synthesis of atomically thin metal oxides, *Science*, 2017, **358**(6361), 332–335.
- 21 T. Yuan, Z. Hu, Y. Zhao, J. Fang, J. Lv, Q. Zhang, Z. Zhuang, L. Gu and S. Hu, Two-Dimensional Amorphous SnOx from Liquid Metal: Mass Production, Phase Transfer, and

- Electrocatalytic CO<sub>2</sub> Reduction toward Formic Acid, *Nano Lett.*, 2020, **20**(4), 2916–2922.
- 22 Y. Masuda, Facet controlled growth mechanism of SnO<sub>2</sub> (101) nanosheet assembled film via cold crystallization, *Sci. Rep.*, 2021, **11**(1), 11304.
- 23 N. Syed, C. K. Nguyen, A. Zavabeti, M. X. Low, X. Wei, V. Krishnamurthi, M. Irfan, W. S. L. Lee, N. M. H. Duong, A. T. Nguyen, *et al.*, Vacuum-Free Liquid-Metal-Printed 2D Semiconducting Tin Dioxide: The Effect of Annealing, *ACS Appl. Electron. Mater.*, 2024, DOI: [10.1021/acsaelm.3c01842](https://doi.org/10.1021/acsaelm.3c01842).
- 24 R. S. Datta, N. Syed, A. Zavabeti, A. Jannat, M. Mohiuddin, M. Rokunuzzaman, B. Yue Zhang, M. A. Rahman, P. Atkin, K. A. Messalea, *et al.*, Flexible two-dimensional indium tin oxide fabricated using a liquid metal printing technique, *Nat. Electron.*, 2020, **3**(1), 51–58, DOI: [10.1038/s41928-019-0353-8](https://doi.org/10.1038/s41928-019-0353-8).
- 25 V. Paolucci, J. De Santis, L. Lozzi, G. Giorgi and C. Cantalini, Layered amorphous a-SnO<sub>2</sub> gas sensors by controlled oxidation of 2D-SnSe<sub>2</sub>, *Sens. Actuators, B*, 2022, **350**, 130890.
- 26 A. Pálincás, G. Kálvin, P. Vancsó, K. Kandrai, M. Szendrő, G. Németh, M. Németh, Á. Pekker, J. S. Pap, P. Petrik, K. Kamarás, L. Tapasztó and P. Nemes-Incze, The composition and structure of the ubiquitous hydrocarbon contamination on van der Waals materials, *Nat. Commun.*, 2022, **13**(1), 6770.
- 27 M. Gobbi, E. Orgiu and P. Samorì, When 2D Materials Meet Molecules: Opportunities and Challenges of Hybrid Organic/Inorganic van der Waals Heterostructures, *Adv. Mater.*, 2018, **30**(18), 1706103.
- 28 T. Daeneke, P. Atkin, R. Orrell-Trigg, A. Zavabeti, T. Ahmed, S. Walia, M. Liu, Y. Tachibana, M. Javaid and A. D. Greentree, Wafer-Scale Synthesis of Semiconducting SnO Monolayers from Interfacial Oxide Layers of Metallic Liquid Tin, *ACS Nano*, 2017, **11**(11), 10974–10983.
- 29 A. Jannat, N. Syed, K. Xu, M. A. Rahman, M. M. M. Talukder, K. A. Messalea, M. Mohiuddin, R. S. Datta, M. W. Khan, T. Alkathiri, B. J. Murdoch, S. Z. Reza, J. Li, T. Daeneke, A. Zavabeti and J. Z. Ou, Printable Single-Unit-Cell-Thick Transparent Zinc-Doped Indium Oxides with Efficient Electron Transport Properties, *ACS Nano*, 2021, **15**(3), 4045–4053.
- 30 A. Zavabeti, P. Aukarasereenont, H. Tuohey, N. Syed, A. Jannat, A. Elbourne, K. A. Messalea, B. Y. Zhang, B. J. Murdoch, J. G. Partridge, M. Wurdack, D. L. Creedon, J. van Embden, K. Kalantar-Zadeh, S. P. Russo, C. F. McConville and T. Daeneke, High-mobility p-type semiconducting two-dimensional β-TeO<sub>2</sub>, *Nat. Electron.*, 2021, **4**(4), 277–283.
- 31 G. Kresse and J. Furthmüller, Efficient iterative schemes for ab initio total-energy calculations using a plane-wave basis set, *Phys. Rev. B: Condens. Matter Mater. Phys.*, 1996, **54**(16), 11169–11186.
- 32 G. Kresse and J. Furthmüller, Efficiency of ab initio total energy calculations for metals and semiconductors using a plane-wave basis set, *Comput. Mater. Sci.*, 1996, **6**(1), 15–50.
- 33 J. P. Perdew, K. Burke and M. Ernzerhof, Generalized Gradient Approximation Made Simple, *Phys. Rev. Lett.*, 1996, **77**(18), 3865–3868.
- 34 P. E. Blochl, Projector Augmented-Wave Method, *Phys. Rev. B: Condens. Matter Mater. Phys.*, 1994, **50**(24), 17953–17979.
- 35 S. Grimme, J. Antony, S. Ehrlich and H. Krieg, A consistent and accurate ab initio parametrization of density functional dispersion correction (DFT-D) for the 94 elements H-Pu, *J. Chem. Phys.*, 2010, **132**(15), 154104.
- 36 Y. Sun, S. Sun, Y. Zheng, Z. Zhang, T. Hou, H. Du and J. Wang, The role of oxygen vacancies on SnO<sub>2</sub> in improving formaldehyde competitive adsorption: A DFT study with an experimental verification, *Appl. Surf. Sci.*, 2021, **570**, 151110.
- 37 D. Wang, Y. Chen, Z. Liu, L. Li, C. Shi, H. Qin and J. Hu, CO<sub>2</sub>-sensing properties and mechanism of nano-SnO<sub>2</sub> thick-film sensor, *Sens. Actuators, B*, 2016, **227**, 73–84.
- 38 X. Wang, H. Qin, Y. Chen and J. Hu, Sensing Mechanism of SnO<sub>2</sub> (110) Surface to CO: Density Functional Theory Calculations, *J. Phys. Chem. C*, 2014, **118**(49), 28548–28561, DOI: [10.1021/jp501880r](https://doi.org/10.1021/jp501880r).
- 39 P. Atkin, R. Orrell-Trigg, A. Zavabeti, N. Mahmood, M. R. Field, T. Daeneke, I. S. Cole and K. Kalantar-zadeh, Evolution of 2D tin oxides on the surface of molten tin, *Chem. Commun.*, 2018, **54**(17), 2102–2105.
- 40 C.-H. Huang, H. Chang, T.-Y. Yang, Y.-C. Wang, Y.-L. Chueh and K. Nomura, Artificial Synapse Based on a 2D-SnO<sub>2</sub> Memristor with Dynamically Tunable Analog Switching for Neuromorphic Computing, *ACS Appl. Mater. Interfaces*, 2021, **13**(44), 52822–52832.
- 41 D. J. Lee, S. Lee and D. Y. Kim, Sturdy memristive switching characteristics of flexible 2D SnO prepared by liquid-to-solid exfoliation, *Ceram. Int.*, 2021, **47**(20), 28437–28443.
- 42 N. Syed, A. Zavabeti, K. A. Messalea, E. Della Gaspera, A. Elbourne, A. Jannat, M. Mohiuddin, B. Y. Zhang, G. Zheng, L. Wang, *et al.*, Wafer-Sized Ultrathin Gallium and Indium Nitride Nanosheets through the Ammonolysis of Liquid Metal Derived Oxides, *J. Am. Chem. Soc.*, 2019, **141**(1), 104–108.
- 43 M. H. Vong, M. Kong, U. Jeong and M. Dickey, *Continuous large area oxide printing from liquid metals*, SPIE, 2023.
- 44 Q. Li, J. Lin, T.-Y. Liu, X.-Y. Zhu, W.-H. Yao and J. Liu, Gas-mediated liquid metal printing toward large-scale 2D semiconductors and ultraviolet photodetector, *npj 2D Mater. Appl.*, 2021, **5**(1), 36.
- 45 Y. Ye, A. B. Hamlin, J. E. Huddy, M. S. Rahman and W. J. Scheideler, Continuous Liquid Metal Printed 2D Transparent Conductive Oxide Superlattices, *Adv. Funct. Mater.*, 2022, **32**(33), 2204235.
- 46 A. B. Hamlin, Y. Ye, J. E. Huddy, M. S. Rahman and W. J. Scheideler, 2D transistors rapidly printed from the crystalline oxide skin of molten indium, *npj 2D Mater. Appl.*, 2022, **6**(1), 16.
- 47 L. Z. Liu, T. H. Li, X. L. Wu, J. C. Shen and P. K. Chu, Identification of oxygen vacancy types from Raman spectra

- of SnO<sub>2</sub> nanocrystals, *J. Raman Spectrosc.*, 2012, **43**(10), 1423–1426.
- 48 P. Pooja, C. C. Che, S.-H. Zeng, Y. C. Lee, T.-J. Yen and A. Chin, Outstanding High Field-Effect Mobility of 299 cm<sup>2</sup> V<sup>-1</sup> s<sup>-1</sup> by Nitrogen-Doped SnO<sub>2</sub> Nanosheet Thin-Film Transistor, *Adv. Mater. Technol.*, 2023, **8**(7), 2201521.
- 49 C. K. Nguyen, M. X. Low, A. Zavabeti, B. J. Murdoch, X. Guo, P. Aukarasereenont, A. Mazumder, A. Dubey, A. Jannat, M. A. Rahman, *et al.*, Atomically Thin Antimony-Doped Indium Oxide Nanosheets for Optoelectronics, *Adv. Opt. Mater.*, 2022, **10**(20), 2200925.
- 50 E. Ciftçyrek, B. Šmíd, Z. Li, V. Matolín and K. Schierbaum, Spectroscopic Understanding of SnO<sub>2</sub> and WO<sub>3</sub> Metal Oxide Surfaces with Advanced Synchrotron Based; XPS-UPS and Near Ambient Pressure (NAP) XPS Surface Sensitive Techniques for Gas Sensor Applications under Operational Conditions, *Sensors*, 2019, **19**(21), 4737.
- 51 C. Li, N. Zhang and P. Gao, Lessons learned: how to report XPS data incorrectly about lead-halide perovskites, *Mater. Chem. Front.*, 2023, **7**(18), 3797–3802.
- 52 A. Singh, M. Vats, S. Mohapatra, M. Tomar, A. Chowdhuri and V. Singh, Template-assisted mesoporous SnO<sub>2</sub> based gas sensor for NO<sub>2</sub> detection at low temperature, *J. Porous Mater.*, 2024, **31**(2), 545–555.
- 53 S. Najmaei, *et al.*, Tailoring the Physical Properties of Molybdenum Disulfide Monolayers by Control of Interfacial Chemistry, *Nano Lett.*, 2014, **14**(3), 1354–1361.
- 54 D.-H. Kang, *et al.*, Controllable Nondegenerate p-Type Doping of Tungsten Diselenide by Octadecyltrichlorosilane, *ACS Nano*, 2015, **9**(2), 1099–1107.